4-2020

Influence of Cr content on the microstructure and mechanical properties of CrxFeNiCu high entropy alloys

Hao Wu

Sirui Huang

Chengyan Zhu

Heguo Zhu

Zonghan Xie
Edith Cowan University, z.xie@ecu.edu.au

10.1016/j.pnsc.2020.01.012
Wu, H., Huang, S., Zhu, C., Zhu, H., & Xie, Z. (2020). Influence of Cr content on the microstructure and mechanical properties of CrxFeNiCu high entropy alloys. *Progress in Natural Science: Materials International, 30*(2), 239 - 245. https://doi.org/10.1016/j.pnsc.2020.01.012

Progress in Natural Science: Materials International 30 (2020) 239–245

HOSTED BY

Contents lists available at ScienceDirect

Progress in Natural Science: Materials International

journal homepage: www.elsevier.com/locate/pnsmi

Original Research

Influence of Cr content on the microstructure and mechanical properties of $Cr_xFeNiCu$ high entropy alloys

Hao Wu[a], Sirui Huang[a], Chengyan Zhu[a], Heguo Zhu[a,*], Zonghan Xie[b,c,**]

[a] College of Materials Science and Engineering, Nanjing University of Science and Technology, Nanjin, 210094, China
[b] School of Mechanical Engineering, University of Adelaide, SA, 5005, Australia
[c] School of Engineering, Edith Cowan University, WA, 6027, Australia

ARTICLE INFO

Keywords:
$Cr_xFeNiCu$ high entropy alloy
First-principle calculations
Microstructure
Mechanical properties
Strengthening mechanism

ABSTRACT

The effect of Cr content on the microstructure and mechanical properties of $Cr_xFeNiCu$ high entropy alloys (HEAs) was firstly studied by first-principles calculations. The calculated results show that the hardness of the alloys increased with the expense of its plasticity decrease, if the content of Cr in the alloy increased. In order to verify the calculated results, $Cr_xFeNiCu$ (x = 0.8, 1, 1.5 and 2) high entropy alloys were synthesized by vacuum induction melting in the present study. The results show that as the value of x increased from 0.8 to 2, the crystal structure changed from single phase face centered cubic (FCC) phase to a mixture of FCC and body centered cubic (BCC) phases. For the single phase FCC (x = 0.8) structure, both the tensile strength and hardness values were low, which were 491.6 MPa and 322.2 HV respectively, however, the plasticity was high, reaching 33.2%. With the formation and growth of BCC phase (x = 2) the tensile strength and hardness of the alloy were significantly improved, which were 872.6 MPa and 808 HV, respectively.

1. Introduction

High entropy alloys (HEAs) have attracted considerable attention in the past decade. Unlike conventional alloys comprising one or two main elements [1,2], HEAs typically contain more than four principal components, which results in high configurational entropy to inhibit the formation of intermetallic compounds and promote the development of simple solid solutions, for instance, body centered cubic (BCC), face centered cubic (FCC) or the mixture of them [1,2]. HEAs have shown excellent physical and mechanical properties, including high strength [3–5] and hardness [6,7], and superior resistance to oxidation [8,9] and corrosion [10–12], thereby heralding a new era for creating high performance structural materials.

The variation of composition in a high-entropy alloy system is expected to have a significant effect on its crystal structure, microstructure and mechanical properties [13–20]. For example, with the increase of Al content, the relative amount of FCC and BCC phases changes in $Al_xCoCrFeNi$ system [13]. The increase of Al content (and the decrease of Ni content) in $CrFeNi_{(3-x)}Al_x$ system saw its strength enhanced, accompanied by the drop of ductility as a result of the alloy being transformed from hypoeutectic to hypereutectic microstructure. Varying the Pd content also affects the microstructure of $CoCrFeMnNiPd_x$ alloy [15]. The results show that with the increase of Pd content, the alloy microstructure transformed from the divorced eutectic to the coarse granular divorced eutectic structure, surrounded by fine flaky dendritic crystals. As the content of Pd continued to increase, the seaweed dendritic pattern emerged.

In recent years, the first-principles calculation based on density functional theory has been used to shed light on the unique properties of the high entropy alloys [21–23]. For example, the thermodynamic properties of the CoCrFeMnNi high entropy alloy (HEA) are probed by first principles calculations [22]. The results show that the contribution of vibration, electron and magnetic entropy contribution must be considered to accurately predict the phase stability in the HEA systems. For $Al_xCrMnFeCoNi$ high-entropy alloy system [23], the effect of Al content on the elastic properties in both body-centered cubic and face-centered cubic structures was simulated. With the increase of Al content, the lattice constant of high entropy alloy is increased. The calculated elastic parameters show that the elastic anisotropy is unusually high in both structures.

It is worth noting that computational simulations have rarely been combined with experiments in the exploration of high entropy alloys. To address this shortcoming a series of $Cr_xFeNiCu$ high entropy alloys were prepared in this work, and the influence of Cr content on their

* Corresponding author. College of Materials Science and Engineering, Nanjing University of Science and Technology, Nanjin, 210094, China.
** Corresponding author. School of Mechanical Engineering, University of Adelaide, SA, 5005, Australia.
E-mail addresses: zhg1200@sina.com, zhg1200@njust.edu.cn (H. Zhu), zonghan.xie@adelaide.edu.au (Z. Xie).

https://doi.org/10.1016/j.pnsc.2020.01.012
Received 13 August 2019; Received in revised form 14 January 2020; Accepted 14 January 2020
Available online 17 February 2020

microstructures and mechanical properties were studied by coupling first-principle calculations with experiments. The strengthening mechanisms were identified and discussed for this alloy system.

2. Computational methods

This work was carried out using the Castep (Cambridge Sequential total energy package) based on density functional theory. The solid solution model was established using the VCA(virtual crystal approximation). Because the high entropy alloy has an incompletely ordered cubic structure, a single cell was employed to build cubic structures and virtual crystal approximations on atoms in the cell so as to avoid errors which may produce "virtual atoms" [24].

The PBE (Perdew burke ernzerhof) of the GGA (generalized gradient approximation) was adopted to create electron exchange association function. The interaction between electron and ion was disposed by the norm-conserving pseudopotential [25] based on the first-principles modelling. The plane truncated energy Ecut was set at 690.0 eV. To ensure the sensitive simulations of the elastic tensor, the energy cutoff was increased to 700.0 eV [26]. The alloy integration was performed using a 12 × 12 × 12 k-point mesh via the Monkhorst-Pack method. The density mixing (Pulay) was applied in self-consistent field and the convergence conditions are given as follows: a) the value of SCF (Self-consistent Field) tolerance is 1.0×10^{-6} eV/atom; b) the value of change mixing amplitude is 0.5; and c) the value of max SCF cycles is 100.

3. Experimental procedures

Chrome particles (purity 99.9%, 1–2 mm in diameter and 5 mm in length), iron particles (purity 99.9%, 1–2 mm in diameter and 5 mm in length), nickel particles (purity 99.9%, 1–2 mm in diameter and 5 mm in length) and copper particles (purity 99.9%, 1–2 mm in diameter and 5 mm in length) were used as starting materials. A series of $Cr_xFeNiCu$ (x = 0.8,1,1.5 and 2) compacts were prepared by a mix of these powders. The green bodies were placed in ceramic crucible before the induction melting in high purity argon. The induced current was set as 500 A. After all particles melted, the magnetic force was used to stir molten metals for about 5 min. The liquid metal was poured into a copper crucible and then cooled down to room temperature.

The phase constitution was detected by X-ray diffraction (XRD) analysis (Bruker-AXS D8 Advance). The microstructures and chemical composition of the four $Cr_xFeNiCu$ alloys were characterized by scanning electron microscope (SEM, FEI Quanta 250 FEG) and energy-dispersive X-ray spectroscopy (EDS, FEI Quanta 250 FEG). The SEM specimens were prepared by mechanical polishing, followed by chemical etching with aqua regia ($HCl:HNO_3$ = 3:1). Image-Pro Plus 6.0 software was employed to measure the grain sizes of the four $Cr_xFeNiCu$ alloys. This was done using the SEM images acquired at 3000 × magnification; at least three SEM images were analysed for each alloy. The volume fractions of FCC and BCC phases were estimated by the Image J software. The transmitted samples were cut into thin slices (0.5 mm) by wire cutting and ground to a thickness of about 40 μm. Three disks were prepared from the thin samples. Subsequently, the specimens were further thinned using ion milling (Gatan 695C) at a voltage of 5 keV with the angle of 6° to be suitable for microstructural analysis under a transmission electron microscope (TEM, TECNAI G2 20 LaB6).

The tensile samples (length ~10.6 mm; width ~2.4 mm; and thickness ~1.2 mm) were wire cut from the ingots. Three samples were prepared for each alloy and tested using UTM/CMT 5000 electronic universal testing machine under a strain rate of 0.5 mm/min at ambient temperature. The fracture surface was observed by SEM. The hardness was measured under a maximum load of 5 N by Vickers hardness tester (HVS-1000). Each specimen was measured at least 5 times for obtaining the average value.

4. Results and discussions

4.1. Phase analysis

In order to build a high-fidelity model for computational simulations, the crystal structure of $Cr_xFeNiCu$ high entropy alloys was tackled. For that, the parameter Ω was proposed to predict whether stable solid phase can form in an alloy [27,28], which is expressed below:

$$\Omega = \frac{T_m \Delta S_{mix}}{|\Delta H_{mix}|} \tag{1}$$

$$T_m = \sum_{i=1}^{n} c_i (T_m)_i \tag{2}$$

$$\Delta S_{mix} = -R \sum_{i=1}^{n} (c_i I n c_i) \tag{3}$$

$$\Delta H_{mix} = 4 \sum_{\substack{i=1 \\ i \neq j}}^{n} \Delta H_{ij}^{mix} c_i c_j \tag{4}$$

where c_i is the atomic percent of the each element, T_m is the melting temperature, R is the gas constant (8.314 $J{\cdot}K^{-1}{\cdot}mol^{-1}$). Besides, $\Delta Hmix\ ij$ is the mixing enthalpy between the i_{th} and j_{th} elements, as pointed out in Fig. 1.

For $Cr_xFeNiCu$ HEAs, T_m, ΔS_{mix}, ΔH_{mix} and Ω are calculated and shown in Table 1. It can be seen that when Cr content increases from 0.8 to 2, the Ω value of $Cr_xFeNiCu$ HEAs moves up from 3.98 to 5.57.

In addition, to appreciate the lattice distortion in the structure, the parameter δ can be used as follows [27,29]:

$$\delta = \sqrt{\sum_{i=1}^{n} c_i \left(1 - \frac{r_i}{r}\right)^2} \tag{5}$$

$$\overline{r} = \sum_{i=1}^{n} r_i c_i \tag{6}$$

where c_i is the atomic percent of each element and r_i is the atomic size of each element (see Fig. 1). δ is calculated and it value is given in Table 2. The criteria for forming a single solid solution are $\Omega > 1.1$ and $\delta < 6.6\%$ [30]. Therefore, the $Cr_xFeNiCu$ high entropy alloy is expected to form solid solution.

The above parameters Ω and δ may predict whether an alloy can form single phase solid solution but are unable to determine the structure of phase. From the viewpoint of electronic structure, Guo [31]

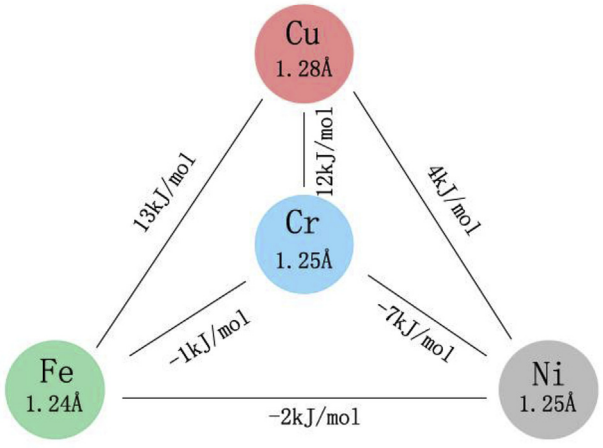

Fig. 1. Values of ΔH_{mix} calculated by Miedema model and atomic sizes of the elements in $Cr_xFeNiCu$ HEA system.

Table 1
T_m, ΔS_{mix}, ΔH_{mix} and Ω of $Cr_xFeNiCu$ HEAs with different x values.

Specimen	T_m, K	ΔS_{mix}, J·K^{-1}·mol^{-1}	ΔH_{mix}, kJ·mol^{-1}	Ω
$Cr_{0.8}FeNiCu$	1747.78	11.49	5.04	3.98
CrFeNiCu	1769.25	11.53	4.75	4.29
$Cr_{1.5}FeNiCu$	1814.77	11.38	4.15	4.98
$Cr_2FeNiCu$	1851.40	11.08	3.68	5.57

Table 2
δ and VEC of $Cr_xFeNiCu$ HEAs with different x values.

Specimen	δ,%	VEC
$Cr_{0.8}FeNiCu$	1.22	8.89
CrFeNiCu	1.20	8.75
$Cr_{1.5}FeNiCu$	1.14	8.44
$Cr_2FeNiCu$	1.08	8.20

proposed that the phase stability of HEAs can be assessed by valence electron concentration (VEC). (Essentially e/a is used to predict the phase stability of HEAs).

$$VEC = \sum_{i=1}^{n} c_i (VEC)_i \tag{7}$$

where VEC is the number of valence electrons per element. In Guo's study, most HEA alloy systems follow the VEC rule. It is found that the FCC is stable when VEC ≥ 8, and the BCC is stable when VEC ≤ 6.87, in-betweens are a mixture of FCC and BCC phases. The VEC of the $Cr_xFeNiCu$ high entropy alloys with different x values were calculated and presented in Table 2, it indicates that the $Cr_xFeNiCu$ high entropy alloy is made of FCC single phase.

4.2. First principles calculation

The elastic constants of metallic materials are described as the stress used to maintain given deformations. Stress [$\sigma_{\alpha\beta}$] and strain [$\varepsilon_{\alpha\beta}$] are considered to be second-order symmetric tensors, which are expressed as σ_i (i = 1, 2, 3, 4, 5, 6) and ε_j (j = 1, 2, 3, 4, 5, 6), respectively. Therefore, the elastic constant C_{ij} can be expressed with a 6 × 6 symmetric coefficient matrix, which connected σ_i and ε_j.

Note that high entropy alloys assuming cubic crystal structure only have three elastic constants. The elastic constants (C_{ij}) of the FCC $Cr_xFeNiCu$ (x = 0.8, 1, 1.5 and 2) high entropy alloys, which are defined as C_{11}, C_{12} and C_{44}, were simulated and the results are listed in Table 3. The elastic constants can be used to evaluate the mechanical stability of the materials, according to the criterion below [32]:

$$C_{11} > 0,\ C_{44} > 0,\ C_{11} - C_{12} > 0,\ C_{11} + 2C_{12} > 0 \tag{8}$$

The Cauchy pressure (C_{12}–C_{44}) is related to the bonding characteristic of the inner part of the structure [33]. The positive value of Cauchy pressure indicates that metal bonds in the material while the negative value suggests covalent bonds. As the content of Cr increases, the Cauchy pressure (C_{12}–C_{44}) is always positive. In addition, the $Cr_{0.8}FeNiCu$ high entropy alloy exhibits the extremely high value of Cauchy pressure among as listed in Table 3, suggesting that the metal bonds are dominant in the alloy.

Table 3
Elastic constants (C_{ij}) of $Cr_xFeNiCu$ HEAs.

Specimen	C_{11}/GPa	C_{12}/GPa	C_{44}/GPa	C_{12}–C_{44}/GPa
$Cr_{0.8}FeNiCu$	245.66	241.73	112.28	129.45
CrFeNiCu	227.36	154.64	112.06	42.58
$Cr_{1.5}FeNiCu$	254.34	107.21	92.89	14.32
$Cr_2FeNiCu$	421.73	119.96	91.68	28.28

Table 4
Bulk modulus B, shear modulus G, Young's modulus E, Poisson's ratio ν and G/B of $Cr_xFeNiCu$ HEAs.

Specimen	B/GPa	G/GPa	E/GPa	ν	G/B
$Cr_{0.8}FeNiCu$	243.04	84.82	227.94	0.34	0.35
CrFeNiCu	178.88	102.39	259.95	0.26	0.57
$Cr_{1.5}FeNiCu$	156.25	107.55	262.44	0.22	0.69
$Cr_2FeNiCu$	220.55	136.05	338.54	0.24	0.62

The bulk modulus B, shear modulus G, Young's modulus E and Poisson's ratio ν of the $Cr_xFeNiCu$ high entropy alloy are calculated, according to Voigt-Reuss-Hill equations below [34]:

$$B = \frac{(C_{11} + 2C_{12})}{3} \tag{9}$$

$$G = \frac{G_V + G_R}{2} \tag{10}$$

$$G_V = \frac{(C_{11} + C_{12} + 3C_{44})}{5} \tag{11}$$

$$G_R = \frac{5(C_{11} - C_{12})C_{44}}{4C_{44} + 3(C_{11} - C_{12})} \tag{12}$$

$$E = \frac{9BG}{3B + G} \tag{13}$$

$$\nu = \frac{3B - 2G}{2(3B + G)} \tag{14}$$

The results are listed in Table 4. The high values of shear and Young's modulus often signify the high hardness and low plasticity [35]. With the increase of Cr content, the shear modulus increased from 84.82 GPa to 136.05 GPa, and the Young's modulus increased from 227.94 GPa to 338.54 GPa. Therefore, the $Cr_{0.8}FeNiCu$ high entropy alloy may have the lowest hardness and highest plasticity, while the $Cr_2FeNiCu$ high entropy alloy may show the opposite pattern.

The ratio of shear modulus to bulk modulus (G/B) can be used to estimate the plasticity of an alloy; that is, when $G/B < 0.57$, the alloy may show a good ductility [36]. As obtained in Table 4, the plasticity of the high entropy alloys decreases as the content of Cr increases. The high entropy alloy $Cr_{0.8}FeNiCu$ may have good ductility. Besides, the Poisson's ratio ν can also be used as a criterion for determining whether materials are brittle. When $\nu > 0.31$, the alloy may exhibit a good ductility [37]. The Poisson's ratio ν of the $Cr_{0.8}FeNiCu$ high entropy alloy again indicates that it is ductile while others might be brittle. However, it is worth pointing out that the strength and plasticity are macroscopic properties of the material, which are determined by various factors. The results of the first principles calculations were used to gain insight of the mechanical properties of the material. In the following sections, the strength, hardness and plasticity of the alloys will be verified by the experiments.

4.3. Microstructure

Fig. 2 shows the XRD diffraction patterns of $Cr_xFeNiCu$ high entropy alloys. With the increase of Cr content the phase constituents changed from single-phase FCC to dual-phase type containing BCC and FCC. Specifically, when the Cr content was less than or equal to 1 (x ≤ 1), only the FCC crystal structure could be observed. However, when the value of x was 1.5 the BCC peak (110) began to appear near FCC peak (111). When the value of x further was increased to 2, the BCC peak became more intensive.

The high entropy alloys (x = 1.5 and 2) comprise FCC + BCC phases, which contradicts the VEC rules. The results indicate that other factors may play an important role. What's more, the phase stability determined by VEC only applies to the system with similar atomic size

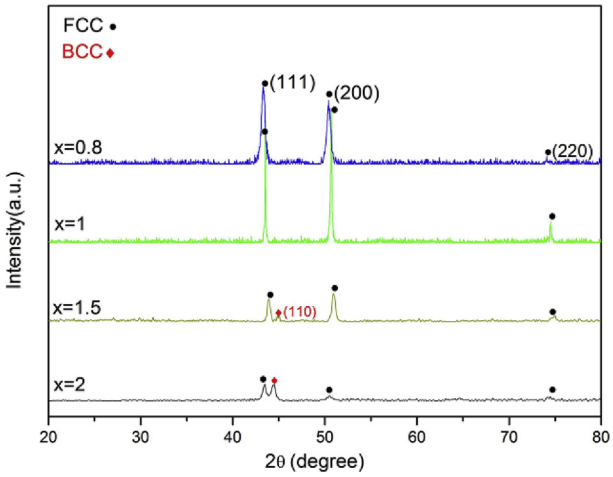

Fig. 2. XRD patterns of $Cr_xFeNiCu$ high entropy alloys with different x values.

[31]. It is also worth noting that the diffraction peak of $Cr_2FeNiCu$ high entropy alloy has a small shift to the left, which may result from the increase of the interplanar crystal spacing caused by the increase of Cr content.

In order to study the phase development with increasing Cr content, the microstructures of $Cr_xFeNiCu$ alloys with different Cr contents were obtained and are shown in Fig. 3. Fig. 3a shows a coarse columnar structure, and Fig. 3b shows a dendritic structure. Both of them are supposed to comprise single phase FCC, according to the XRD analysis in Fig. 2. Fig. 3(c and d) reveals the microstructures of x = 1.5 and x = 2 alloys, respectively. Fig. 3c shows a fine, more equiaxed dendritic structure, while Fig. 3d shows a much finer structure. In Fig. 3c, a small number of dark regions (which were found to be BCC phase likely [38]) were found. When the content of Cr continued to increase, these dark regions expanded. That is because that the volume fraction of BCC phase increases gradually, accompanied by the decrease in the volume of FCC phase decrease.

The EDS results in Table 5 show that both the FCC phase (area A) and the BCC phase (area B) were enriched in Cr and Fe, while the crystal boundaries (area C) were enriched in Cu. By contrast, Ni elements evenly distributed throughout the samples. The Cu element segregation in the crystal boundaries can be explained by the ΔH_{mix} between Cu atoms and other atoms [39]. The ΔH_{mix} of Cu–Cr,Cu–Fe and Cu–Ni were 12 kJ/mol、13 kJ/mol and 4 kJ/mol, respectively (Fig. 1). The ΔH_{mix} of Cu–Ni was significantly lower than others. Therefore, Cu element tended to segregate at the crystal boundaries, rather than stayed within the grains where Cr and Fe were concentrated.

Table 5
Chemical compositions of $Cr_xFeNiCu$ HEA by SEM/EDS (areas marked in Fig. 3).

Specimen	Nominal composition	Area	Element (at.%)		Ni	Cu
			Cr	Fe		
$Cr_{0.8}FeNiCu$	$Cr_{21.1}Fe_{26.3}Ni_{26.3}Cu_{26.3}$	A	26.80	31.90	29.77	11.53
		C	9.06	9.02	16.36	65.56
CrFeNiCu	$Cr_{25}Fe_{25}Ni_{25}Cu_{25}$	A	29.95	30.90	27.17	11.98
		C	9.72	10.18	19.18	60.92
$Cr_{1.5}FeNiCu$	$Cr_{33.4}Fe_{22.2}Ni_{22.2}Cu_{22.2}$	A	32.04	28.28	27.14	12.54
		B	33.09	28.38	26.23	12.30
		C	11.12	16.13	20.15	52.6
$Cr_2FeNiCu$	$Cr_{40}Fe_{20}Ni_{20}Cu_{20}$	A	33.87	24.01	30.95	11.17
		B	50.84	24.26	18.75	6.15
		C	19.99	9.06	11.53	59.42

TEM analysis reveals detailed microstructure and phase composition of the $Cr_xFeNiCu$ HEA. The diffraction pattern of FCC solid solution is shown in Fig. 4a. In comparison, the diffraction patterns of both FCC and BCC solid solutions are displayed in Fig. 4b. The lattice planes are also indexed.

4.4. Mechanical properties

Fig. 5 shows the engineering stress-strain curves of the $Cr_xFeNiCu$ alloys. It can be seen that with increasing Cr content, the tensile strength of the alloys increased, while the elongation-to-failure

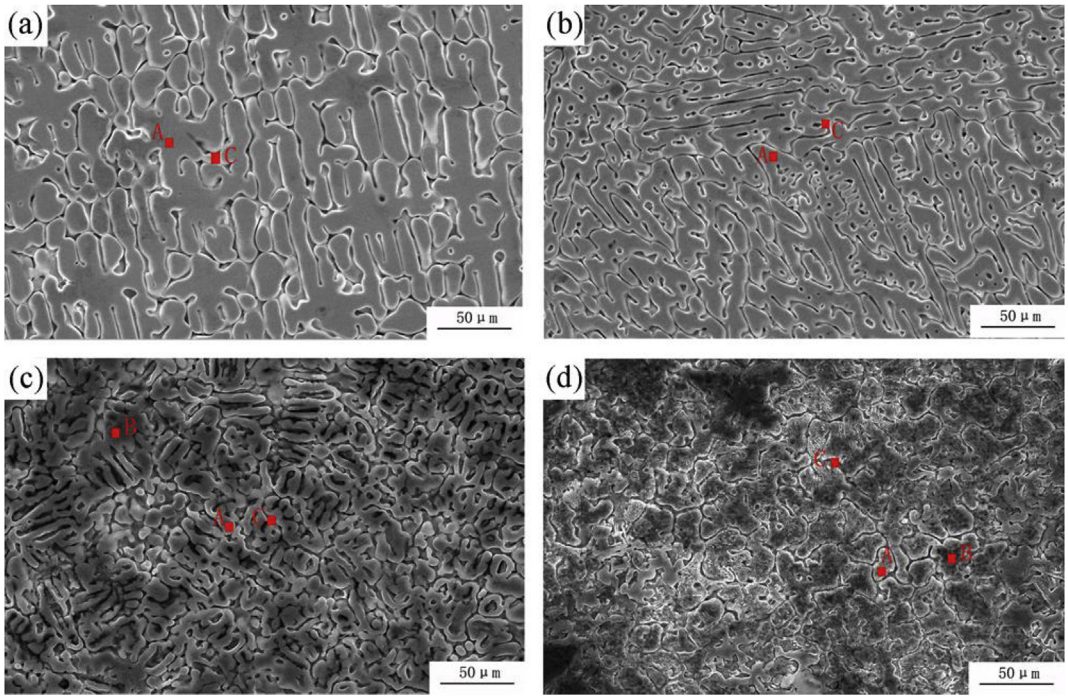

Fig. 3. Microstructure of $Cr_xFeNiCu$ alloy with different x values, (a) x = 0.8; (b) x = 1; (c) x = 1.5; and (d) x = 2.

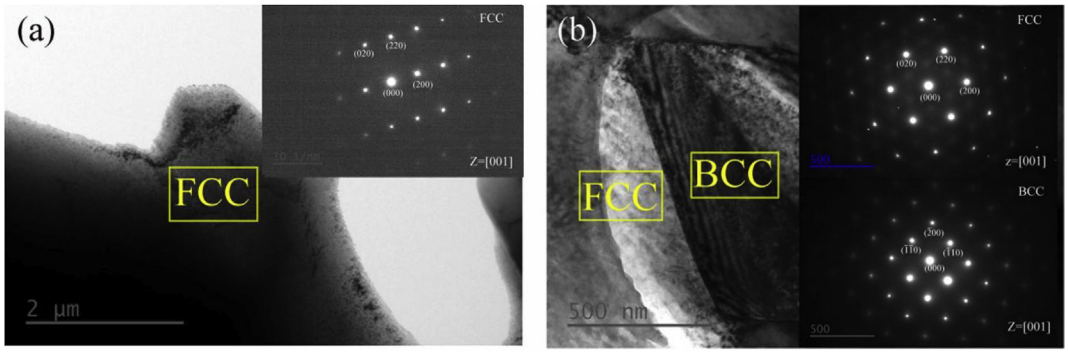

Fig. 4. TEM image and selected area electron diffraction of the $Cr_xFeNiCu$ HEA, (a) x = 1 and (b) x = 2.

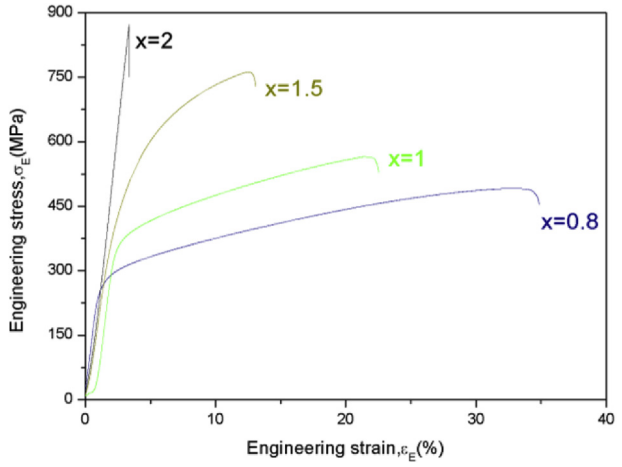

Fig. 5. Engineering stress-strain curves of $Cr_xFeNiCu$ HEAs with different x values.

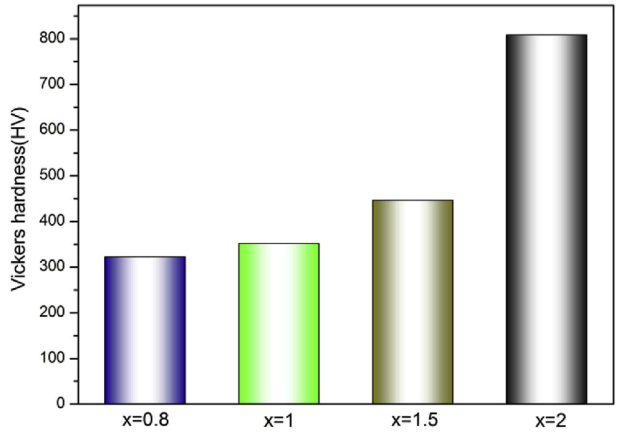

Fig. 6. Microhardness of $Cr_xFeNiCu$ HEAs with different x values.

decreased. The hardness values of the $Cr_xFeNiCu$ high entropy alloys with different Cr contents were also investigated and the results are reported in Fig. 6. It shows that with the increase of Cr content, the hardness increased from 322.2 HV to 808 HV. The results indicate that the Cr variation has a significant effect on the tensile properties of the $Cr_xFeNiCu$ high entropy alloy system. When x = 0.8, the alloy had a single FCC structure, its tensile strength was 491.6 MPa and its elongation-to-failure was 33.2%. When the value of x increased to 1, the tensile strength was 565.5 MPa while the elongation was 21.5%. When the value of x increased to 1.5, the tensile strength and elongation-to-failure of the alloy were 761.8 MPa and 12.6%, respectively. As the value of x increased further to 2, the tensile strength of the $Cr_2FeNiCu$ high entropy alloy was 1.78 times higher than that of single-phase FCC alloy for $Cr_{0.8}FeNiCu$ high entropy alloy, while its plasticity reduced considerably to 3.3%.

A number of strengthening mechanisms have been found in high entropy alloys [4,5,14,17]. For most of them, the plastic deformation depends on dislocation slip. Therefore, the factors that resist the dislocation slip can improve the strength of the materials.

Solid solution strengthening is often seen as one of primary strengthening mechanisms for high entropy alloys, which is mainly realized by the uniform distribution of constituent atoms. When Cr atoms are dissolved in the matrix to form solid solution, lattice distortion is expected to occur in the matrix. The stress field caused by lattice distortion interacts with the stress field around the dislocations, which making the dislocations motion more difficult to take place. Consequently, the shear stress required for the dislocation slip increase in order to overcome such pinning effect. In addition, the solute atoms might segregate around stacking faults, further blocking the movement of dislocations. The tensile strength rise $\Delta\sigma_{solute}$ due to the solid solution strengthening can be expressed as [40]:

$$\Delta\sigma_{solute} = G\varepsilon\left(\frac{X_f}{4}\right)^{\frac{1}{2}} \tag{15}$$

where G is the shear modulus of the alloy, ε is the difference in the diameter between the parent atoms and the solute atoms (refer to the previous dates in Fig. 1), and X_f is the concentration of the solute atoms. When the value of x increases, the values of G (refer to the previous simulation in Table 4) and X_f increase as well. Hence, the increase of Cr content can lead to a higher degree of the solid solution strengthening effect.

The grain size in this work was found to decrease with the increase of x value, as shown in Fig. 7a. The decrease of grain size is known to increase grain boundary area and boost the resistance to dislocation movement, thereby raising the strength of high entropy alloys. The yield stress σ_s can be calculated according to the classical Hall-Petch equation [41–43]:

$$\sigma_s = \sigma_0 + K_s d^{-\frac{1}{2}} \tag{16}$$

where σ_s and σ_0 are the yield stress and lattice friction stress, K_s is constant and d is the average diameter of grains. If the grain size changes from d_1 to d_2, a change of the strength would result and can be given as [41]:

$$\Delta\sigma_s = K_s\left(d_2^{\frac{1}{2}} - d_1^{-\frac{1}{2}}\right) \tag{17}$$

As the value of x increases from 0.8 to 2, the average grain size of the alloys decreases from 25.3 μm to 8.9 μm, indicating that the Hall-Petch effect plays an important role in the strengthening mechanism of the alloys.

The structural strengthening also plays an important part in this work. As the value of x increased the volume fraction of the BCC phase

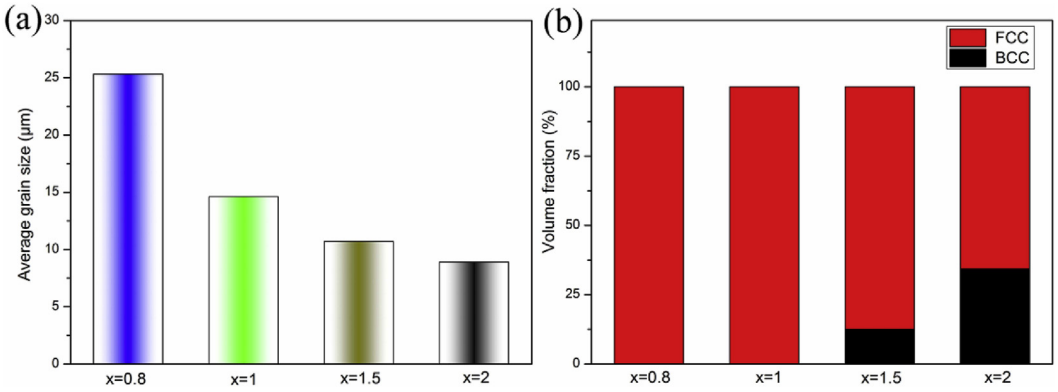

Fig. 7. (a) Average grain sizes of $Cr_xFeNiCu$ HEAs with different x values (b) Volume fractions of FCC and BCC phases of $Cr_xFeNiCu$ HEAs with different x values.

increased, and at the same time the volume fraction of FCC decreased, as shown in Fig. 7b. When the values of x were 0.8 and 1, the volume fraction of the FCC was 100%. As the value of x increased to 1.5, the volume fraction of the BCC increased from 0 to 12.5%. With a further increase of the value of x to 2, the volume fraction of the BCC increased to 34.3%. For $Cr_xFeNiCu$ high entropy alloys, the structural strengthening σ_{struc} can be given as follows [44]:

$$\sigma_{struc} = \sigma_{FCC} \times V_{FCC} + \sigma_{BCC} \times V_{BCC} \quad (18)$$

where σ_{struc} is the tensile strength, V_{FCC} and V_{BCC} are the volume fractions of FCC phase and BCC phases, respectively. Due to the fact that the BCC phase has a greater strength and lower ductility than the FCC phase ($\sigma_{BCC} > \sigma_{FCC}$) [45,46], the structural strengthening became apparent as the volume fraction of the BCC increased.

The SEM images of the tensile fractured surfaces of $Cr_xFeNiCu$ high entropy alloys are shown in Fig. 8a and Fig. 8b, respectively, for x = 0.8 and x = 1. Many small dimples were observed on the fracture surface, which were fibrous and showed typical ductile fracture. When the value of x was 1.5, the dimples became smaller in size and fluvial patterns appeared, as seen Fig. 8c, which represent a mix of ductile and brittle fracture. With the further increase of Cr content, the fracture surface of the high entropy alloy showed typical brittle fracture characteristics. As seen in Fig. 8d, no dimple structure was found, indicating a brittle failure mode. The previous study [47] has explained this phenomenon with respect of dislocation motion. The number of slip system in the FCC structure is more than that of the BCC, and the stacking fault energy is also higher, so plastic deformation can take place readily in the FCC-dominated structure.

5. Conclusions

A series of $Cr_xFeNiCu$ (x = 0.8, 1, 1.5 and 2) high entropy alloys have been prepared by vacuum induction melting. The influence of Cr content on the phase formation, tensile strength and ductility of the alloys is addressed.

1) With the increase of Cr content, the $Cr_xFeNiCu$ high entropy alloys exhibit a change in phase composition from FCC single phase to FCC + BCC dual phase. Moreover, Cu segregates at the crystal boundaries.
2) With the value of x increasing from 0.8 to 2, the strength and hardness of the high entropy alloys are significantly enhanced and

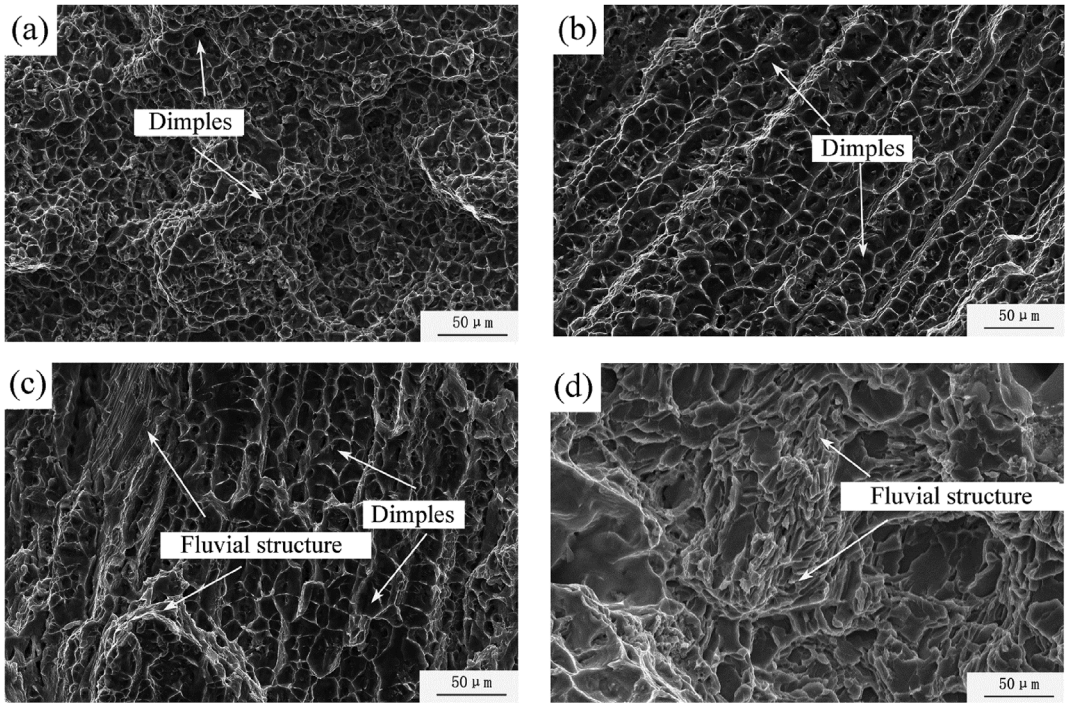

Fig. 8. Fracture surfaces of $Cr_xFeNiCu$ alloys with different x values, (a) x = 0.8; (b) x = 1; (c) x = 1.5 and (d) x = 2.

the plasticity reduced, which is consistent with the simulation results. Specifically, the tensile strength increases from 491.6 MPa to 872.6 MPa, and the Vickers hardness rises from 322.2 HV to 808 HV. The fracture surface shows a transition from ductile to brittle failure pattern. The ductility of the alloys is also in line with the simulation results.

3) The solution strengthening, grain boundary strengthening and structural strengthening are the main strengthening mechanisms identified in this high entropy alloy system. In particular, the increase of Cr content results in the increase in volume fraction of BCC, which plays an important role in strengthening to the alloys.

Declaration of competing interest

None.

Acknowledgment

This work was supported by the National Natural Science Foundation of China (No. 51571118, and No. 51371098) and the Natural Science Foundation of Jiangsu Province (No. BK20141308). Jiangsu Province Science and Technology Plan Project (BE2018753/KJ185629). Z Xie acknowledges the support of the Australian Research Council Discovery Projects.

Appendix A. Supplementary data

Supplementary data to this article can be found online at https://doi.org/10.1016/j.pnsc.2020.01.012.

References

[1] P.K. Huang, J.W. Yeh, T.T. Shun, S.K. Chen, Adv. Eng. Mater. 6 (2004) 74–78.
[2] J.W. Yeh, S.K. Chen, S.J. Lin, J.Y. Gan, T.S. Chin, T.T. Sun, C.H. Tsau, S.Y. Chang, Adv. Eng. Mater. 6 (2004) 299–303.
[3] Z.M. Li, K.G. Pradeep, Y. Deng, D. Raabe, C.C. Tasan, Nature 534 (2016) 227–230.
[4] Z. D Han, X. Liu, S.F. Zhao, Y. Shao, J.F. Li, K.F. Yao, Prog. Nat. Sci.: Met. Mater. Int. 25 (2015) 365–369.
[5] T. Yang, Y.L. Zhao, Y. Tong, Z.B. Jiao, J. Wei, J.X. Cai, X.D. Han, D. Chen, A. Hu, J.J. Kai, K. Lu, Y. Liu, C.T. Liu, Science 362 (2018) 933–937.
[6] J.X. Hou, M. Zhang, H.J. Yang, J.W. Qiao, Y.C. Wu, Mater. Lett. 238 (2019) 258–260.
[7] J.T. Fan, L.J. Zhang, P.F. Yu, M.D. Zhang, D.J. Liu, Z. Zhou, P. Cui, M.Z. Ma, Q. Jing, G. Lia, R.P. Liu, Mater. Sci. Eng. 728 (2018) 30–39.
[8] O.N. Senkov, S.V. Senkova, D.M. Dimiduk, C. Woodward, D.B. Miracle, J. Mater. Sci. 47 (2012) 6522–6534.
[9] Y.S. Huang, L. Chen, H.W. Lui, M.H. Cai, J.W. Yeh, Mater. Sci. Eng. 457 (2007) 77–83.
[10] P. Lu, J.E. Saal, G.B. Olson, T.S. Li, O.J. Swanson, G.S. Frankel, A.Y. Gerard, K.F. Quiambao, J.R. Scully, Scripta Mater. 153 (2018) 19–22.
[11] K.F. Quiambao, S.J. McDonnell, D.K. Schreiber, A.Y. Gerard, K.M. Freedy, P. Lu, J.E. Saal, G.S. Frankel, J.R. Scully, Acta Mater. 164 (2019) 362–374.
[12] H. Luo, Z.M. Li, A.M. Mingers, D. Raabe, Corrosion Sci. 134 (2018) 131–139.
[13] S. Gangireddy, B. Gwalani, V. Soni, R. Banerjee, R.S. Mishra, Mater. Sci. Eng. 739 (2019) 158–166.
[14] M. Muralin, S.P. Kumaresh Babu, B. Jeevan Krishna, A. Vallimanalan, Prog. Nat. Sci.: Met. Mater. Int. 26 (2016) 380–384.
[15] Y.M. Tan, J.S. Li, J. Wang, M. Kolbe, H.C. Kou, J. Alloys Compd. 731 (2018) 600–611.
[16] J. Chen, P.Y. Niu, Y.Z. Liu, Y.K. Lu, X.H. Wang, Y.L. Peng, J.N. Liu, Mater. Des. 94 (2016) 39–44.
[17] R. Wei, H. Sun, Z.H. Han, C. Chen, T. Wang, S.K. Guan, F.S. Li, Mater. Lett. 219 (2018) 85–88.
[18] Z.W. Wang, I. Baker, Z.H. Cai, S. Chen, J.D. Poplawsky, W. Guo, Acta Mater. 120 (2016) 228–239.
[19] T. Borkar, V. Chaudhary, B. Gwalani, D. Choudhuri, C.V. Mikler, V. Soni, T. Alam, R.V. Ramanujan, R. Banerjee, Adv. Eng. Mater. 19 (2017) 1700048.
[20] V. Chaudhary, B. Gwalani, V. Soni, R.V. Ramanujan, R. Banerjee, Sci. Rep. 8 (2018) 15578.
[21] F.Y. Tian, L. Delczeg, N.X. Chen, L.K. Varga, J. Shen, L. Vitos, Phys. Rev. B 88 (2013) 1336–1340.
[22] D.C. Ma, B. Grabowski, F. Körmann, J. Neugebauer, D. Raabe, Acta Mater. 100 (2015) 90–97.
[23] H.L. Zhang, X. Sun, S. Lu, Z.H. Dong, X.D. Ding, Y.Z. Wang, L. Vitos, Acta Mater. 155 (2018) 12–22.
[24] L. Bellaiche, D. Vanderbilt, Phys. Rev. B 61 (2000) 7877–7882.
[25] D.H. Hamalm, M. Schluter, C. Chiang, Phys. Rev. Lett. 43 (1979) 1494–1497.
[26] N.E. Koval, J.I. Juaristic, R.D. Muiñoa, M. Alducin, Intermetallics 106 (2019) 130–140.
[27] X. Yang, Y. Zhang, Mater. Chem. Phys. 132 (2012) 233–238.
[28] X. Yang, S.Y. Chen, J.D. Cotton, Y. Zhang, J. Occup. Med. 66 (2014) 2009–2020.
[29] Y. Zhang, Y.J. Zhou, J.P. Lin, G.L. Chen, P. Liaw, Adv. Eng. Mater. 10 (2008) 534–538.
[30] C. Ng, S. Guo, J. Luan, S.Q. Shi, C.T. Liu, Intermetallics 31 (2012) 165–172.
[31] S. Guo, N.G. Chun, J. Lu, C.T. Liu, J. Appl. Phys. 109 (2011) 103505.
[32] J.F. Nye, Physical Properties of Crystals, Oxford University Press, Oxford, 1985.
[33] D. Nguyen-manh, M. Mrovec, S.P. Fitzgerald, Mater. Trans. 49 (2008) 2497–2506.
[34] O.L. Anderson, J. Phys. Chem. Solid. 24 (1963) 909–917.
[35] L. Gao, J. Zhou, Z.M. Sun, R.S. Chen, E.H. Han, Chin. Sci. Bull. 56 (2011) 1142–1146.
[36] M. Mattesini, R. Ahuja, B. Johansson, Phys. Rev. B 68 (2003) 184108.
[37] X.J. Gu, A.G. McDermott, S.J. Poon, Appl. Phys. Lett. 88 (2006) 211905.
[38] I. Basu, V. Ocelík, J.D. Hosson, Acta Mater. 157 (2018) 105–113.
[39] B. Gwalani, D. Choudhuri, V. Soni, Y. Ren, M. Styles, J.Y. Hwang, S.J. Nam, H. Ryu, S.H. Hong, R. Banerjee, Acta Mater. 129 (2017) 170–182.
[40] X.Z. Zhang, T.J. Chen, Y.H. Qin, Mater. Des. 99 (2016) 182–192.
[41] E.O. Hall, Proc. Phys. Soc. B 64 (1951) 747–753.
[42] N.J. Petch, J. Iron Steel Inst. (1953) 174.
[43] B. Gwalani, Vishal Soni, Michael Lee, S.A. Mantri, Yang Ren, R. Banerjee, Mater. Des. 121 (2017) 254–260.
[44] N.D. Stepanov, N.Y. Yurchenko, D.V. SKibin, M.A. Tikhonovsky, G.A. Salishchev, J. Alloys Compd. 652 (2015) 266–280.
[45] J.Y. He, W.H. Liu, H. Wang, Y. Wu, X.J. Liu, T.G. Nieh, Z.P. Lu, Acta Mater. 62 (2014) 105–113.
[46] Y.X. Zhuang, X.L. Zhang, X.Y. Gu, J. Alloys Compd. 743 (2018) 514–522.
[47] J.J. Harwood, Proceedings of the ASM Seminar: Strengthening Mechanisms in Solids, (1960), p. 23 Metals Park, OH.